Research article

Carbon Future

Covalently bonded TiO_2/graphene interfaces: Interplay between structure, electronic properties, and photocatalytic activity revealed by computational studies

Manasi R Mulay [1,2,†] and Natalia Martsinovich [1] ✉

[1] *Chemistry, School of Mathematical and Physical Sciences, University of Sheffield, Sheffield, S3 7HF, UK*
[2] *Grantham Centre for Sustainable Futures, University of Sheffield, Sheffield, S3 7RD, UK*
[†] *Present address: Department of Metallurgical and Materials Engineering, COEP Tech University, Wellesley Rd, Shivajinagar, Pune, Maharashtra 411005, India*

Cite This: *Carbon Future* **2026**, *3*, 9200071

Read Online

ABSTRACT: Composites of TiO_2 with graphene and other carbon-based nanomaterials are widely used as photocatalysts, since they improve the efficiency of TiO_2 photocatalysts by reducing charge recombination and extending TiO_2 light-harvesting to the visible range. However, the exact nature of binding at TiO_2/graphene interfaces is still unclear. Experimental studies show that Ti–C and Ti–O–C covalent bonds are often present in TiO_2/graphene heterostructures. In this study, we used density functional theory to investigate the nature of binding at the interfaces of graphene with the anatase polymorph of TiO_2. We investigated graphene binding with both the most stable (101) surface of anatase and the less stable but more photocatalytically active (100) and (001) surfaces, and analysed the electronic properties of these interfaces. We found that pristine graphene binds to anatase surfaces by physisorption, while graphene with carbon vacancies can form covalent bonds to TiO_2. The presence of these covalent bonds alters the electronic structure of TiO_2/graphene composites, creating hybridised states that may facilitate charge transfer and hinder electron–hole recombination. This study highlights the important role of defects, such as vacancies, in creating interfacial covalent bonds that may be responsible for the high photocatalytic activity of TiO_2/graphene heterostructures.

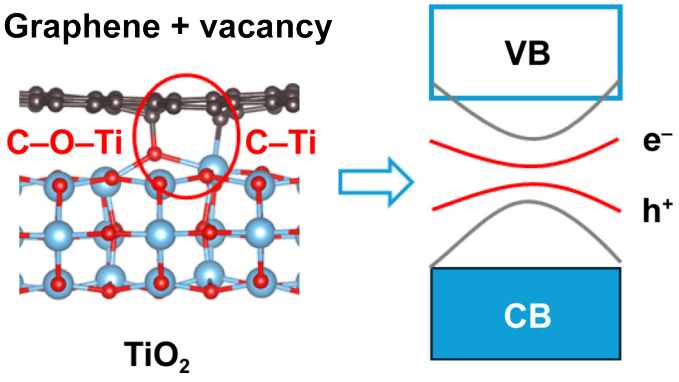

KEYWORDS: photocatalysis, TiO_2, graphene, interface, heterojunction, electronic structure

1 Introduction

Photocatalysis has received a lot of attention as a light-driven process which enables chemical reactions that are otherwise kinetically or thermodynamically unfeasible. Areas of application of photocatalysis range from nature-inspired artificial photosynthesis process[1, 2] and CO_2 reduction processes for carbon capture[3–5] to hydrogen production by photocatalytic water splitting[6–8] and photocatalytic purification of air and water[9–12]. Since sunlight is abundantly available in nature, solar energy driven photocatalysis is seen as a promising method for producing renewable energy and eliminating pollution.

Received: November 4, 2025; **Revised:** March 3, 2026
Accepted: March 13, 2026

✉Address correspondence to Natalia Martsinovich, n.martsinovich@sheffield.ac.uk

https://doi.org/10.26599/CF.2026.9200071

TiO_2 is the most widely used photocatalyst because of its good photocatalytic performance, attributed to efficient generation of electron–hole pairs, high electron mobility, as well as factors such as non-toxicity and stability over reuse cycles[13–16]. However, TiO_2 photocatalysts have two important drawbacks: rapid electron–hole recombination, which results in loss of photogenerated charges, and a large band gap, which means that pure TiO_2 photocatalysts can work only in the ultraviolet (UV) region of the solar spectrum. Multiple strategies have been researched to circumvent these drawbacks by methods such as doping, use of molecular sensitisers, and formation of heterostructures or composites[16–18].

In particular, the formation of heterostructures of TiO_2 with carbon nanomaterials, such as carbon nanotubes, graphene, or reduced graphene oxides, was found to be effective in making TiO_2 active in the visible range and reducing recombination, resulting in greatly improved photocatalytic performance[19–21]. For example, Yang et al. observed a reduction in bandgap from 3.29 eV for commercial TiO_2 (P25) to 2.56 eV in a TiO_2/graphene porous

nanocomposite, proving the TiO_2/graphene nanocomposite to be more efficient in harvesting the visible range of the solar spectrum. They reported 2.6 times higher photocurrent in TiO_2/graphene compared to commercial P25 TiO_2, resulting in 6 times more efficient degradation of methylene blue dye under visible light compared to P25[22]. Mehta et al. reported 13-fold increase in photocurrent density for a TiO_2/graphene nanocomposite compared to pure TiO_2[23]. Liu et al. reported a drastic increase in hydrogen evolution rate from ~ 6 μmol/h for pure TiO_2 photocatalyst to 193 μmol/h for the most reactive anatase TiO_2(100) surface with graphene[24]. This improvement in photocatalytic activity has been attributed to a combination of factors, including graphene's excellent charge carrier mobility, optical absorption, large surface area and adsorption capacity, and efficient transfer of photogenerated electrons between TiO_2 and graphene[22–28]. The addition of nanostructured carbon, such as graphene, to TiO_2 provides higher surface area for catalytic reactions[28]. Photosensitisation of TiO_2 using graphene with its narrow bandgap enables more efficient harvesting of visible light[22, 23, 26, 28]. Furthermore, nanostructured carbon such as graphene enables charge separation between TiO_2 and graphene, acts as charge transport medium, and prevents electron–hole recombination[22–28].

Multiple studies highlighted the key role of interfacial bonding at TiO_2/graphene interfaces in improving the electronic properties which lead to enhanced photocatalytic performance. In particular, a number of studies reported the presence of Ti–O–C[26, 28–35] and Ti–C bonds[22, 24–27, 29–38] in X-ray photoemission spectroscopy (XPS) and Fourier transform infrared (FT-IR) spectroscopy studies of TiO_2/graphene composites. These bonds are believed to act as chemical anchors between graphene and TiO_2 surfaces. Other XPS studies observed Ti–O–C bonds at TiO_2/graphene interfaces, but reported an absence of Ti–C bonds, concluding that TiO_2 and graphene are bridged only by Ti–O–C bonds[39–41]. A study by Min et al. using two different graphene oxide materials with different degrees of oxidation reported the formation of two types of TiO_2/graphene composites: chemically bonded composites with Ti–C and Ti–O–C signals in C 1s and Ti 2p XPS spectra and physisorbed composites with no such bonds[29]. While both types of composites displayed narrowed band gaps and improved photocatalytic efficiencies in decomposing methylene blue compared to P25 TiO_2, the chemisorbed composites displayed narrower band gaps (2.27 eV) and higher photocatalytic degradation rates than the physisorbed composites, highlighting the beneficial role of interfacial bonding[29]. A study by Liu et al. revealed crystal-facet-dependent behaviour in anatase/graphene covalently bonded composites, where (101) and (001) facets of anatase TiO_2 were bonded to graphene mainly through Ti–O–C bonds, while (001) facets were bonded through Ti–C bonds and showed the highest activity in photocatalytic hydrogen production[24]. Overall, photocatalysis studies systematically showed high photocatalytic performance of chemically bonded TiO_2/graphene composites[22, 24–27, 29–37, 39–42]. This high performance was attributed to the interfacial Ti–C and Ti–O–C bonds acting as bridges for transfer of photoexcited electrons from TiO_2 to graphene, facilitating separation of charges and reducing electron–hole recombination[24, 25, 37].

Theoretical studies of interactions between TiO_2 and graphene are necessary, to gain deeper understanding of the nature of binding and charge-transfer processes at these interfaces and to use these insights to design efficient photocatalysts. Theoretical studies of TiO_2/graphene interfaces have mainly focussed on the adsorption of small TiO_2 clusters[43, 44], physisorbed interfaces of pristine graphene and TiO_2[37, 38, 45–50], and adsorption of oxidised graphene on TiO_2[46, 47, 49, 51], with few studies reporting covalent Ti–C bond formation between graphene and TiO_2[37, 38]. There is as yet no clear understanding of the conditions required to form chemical bonds at TiO_2/graphene interfaces.

In this work, we aim to elucidate the nature of interactions at TiO_2/graphene interfaces and systematically explore the possibility of covalent bond formation at interfaces between graphene and anatase, exposing the stable (101) facets and the more reactive (001) and (100) facets. We consider both defect-free and vacancy-containing graphene and find that the presence of vacancies in graphene can lead to the formation of interfacial covalent bonds to TiO_2. Next, we analyse the interplay between structures and electronic properties of physisorbed and covalently bonded TiO_2/graphene composites and find that interfacial covalent bonds give rise to hybridised electronic trap states, which may facilitate the separation of photogenerated charges and therefore can enhance the photocatalytic properties of covalently bonded TiO_2/graphene composites.

2 Method

Interfaces of TiO_2 with graphene were modelled using density functional theory (DFT). Geometry optimisations were performed using CP2K software[52] with the generalized gradient approximation (GGA) Perdew–Burke–Ernzerhof (PBE) functional[53] and Grimme's D3 empirical dispersion correction[54], using double-zeta valence polarised basis sets and Goedecker–Teter–Hutter pseudopotentials,[55] in the Γ-point approximation. All structures were modelled as two-dimensional (2D) periodic systems, with cell heights of 50 Å in the vertical (non-periodic) direction. Positions of all atoms were fully optimised until the maximum displacement was below 0.003 Bohr, root-mean-square displacement below 0.0015 Bohr, maximum force below 0.00045 Bohr/Ha, and root-mean-square force below 0.0003 Bohr/Ha. Lattice parameters were kept fixed at TiO_2 bulk values. Interfacial binding energies E_{bind} were calculated as a difference between the energies of TiO_2/graphene structures and isolated optimised TiO_2 and graphene (Eq. 1)

$$E_{bind} = E_{TiO_2/G} - E_{TiO_2} - E_G + E_{BSSE} \quad (1)$$

where $E_{TiO_2/G}$ is the energy of the TiO_2/graphene heterostructure, E_{TiO_2} is the energy of the isolated optimised TiO_2 slab, E_G is the energy of the isolated optimised graphene sheet, and E_{BSSE} is the basis set superposition error correction calculated using the counterpoise method[56]. Three-dimensional plots of electron density differences $\Delta\rho$ were calculated as a difference between the electron densities of TiO_2/graphene and isolated TiO_2 and graphene (Eq. 2)

$$\Delta\rho = \rho_{TiO_2/G} - \rho_{TiO_2} - \rho_G \quad (2)$$

where $\rho_{TiO_2/G}$ is the electron density of the TiO_2/graphene heterostructure, and ρ_{TiO_2} and ρ_G are the electron densities of the isolated TiO_2 slab and isolated graphene sheet, respectively, in the same geometries as the TiO_2/graphene heterostructure.

Structures optimised using CP2K were further used for calculations of electronic properties (band structures and densities of electronic states) with CRYSTAL17 software[57] using HSE06

hybrid functional[58, 59], Grimme D2 empirical dispersion correction[60], and all-electron triple-zeta valence-polarised basis sets. The structures were modelled as 2D periodic systems, with cell height of 500 Å in the non-periodic direction. Wavefunctions were initially calculated using the 4 × 4 × 1 *k*-point mesh. For calculations of densities of electronic states, the density of *k*-points was increased to 12 × 12 × 1; 1800 points (or 2400 points for TiO_2(100)-based structures) were used in the energy range between −0.5–0.1 Ha; and densities of states were expanded using 10 Legendre polynomials. Band structures were calculated along the path Γ–X–M–Y–Γ, with 20 points along each segment, for the highest 40 occupied bands and the lowest 40 unoccupied bands.

3 Results and discussion

3.1 Structures of TiO_2/graphene heterointerfaces

Since TiO_2 anatase nanoparticles can be controllably synthesised to display various crystallographic facets, from the most stable (101) facet to the more reactive (100) and (001) facets[61], we constructed interfaces of graphene with (101), (100), and (001)-oriented anatase slabs. To create commensurate interfaces, graphene unit cell was matched with the anatase surface unit cells to find the lowest common multiples of the cell parameters, similar to the procedure used in our earlier study[48], as schematically shown in **Fig. 1a** for the anatase TiO_2(101)/graphene interface (further referred to as anatase(101)/graphene or T101/G). Interfaces were considered commensurate if lattice mismatch was below 4%. The dimensions of TiO_2 supercells were fixed, while the dimensions of graphene supercells were adjusted to match the TiO_2 supercells. Sizes of the commensurate supercells used in this study are summarised in **Table 1**.

The smallest commensurate supercell of anatase(101)/graphene (Fig. 1b) was found to be a combination of 2 × 2-extended anatase(101) and 5 × 3-extended graphene cell, with the dimensions of 10.38 Å × 7.64 Å. We used anatase(101) slabs with three Ti_2O_4 repeat layers, so that the anatase(101)/graphene supercell used in this study contained 102 atoms (24 TiO_2 units and 30 C atoms).

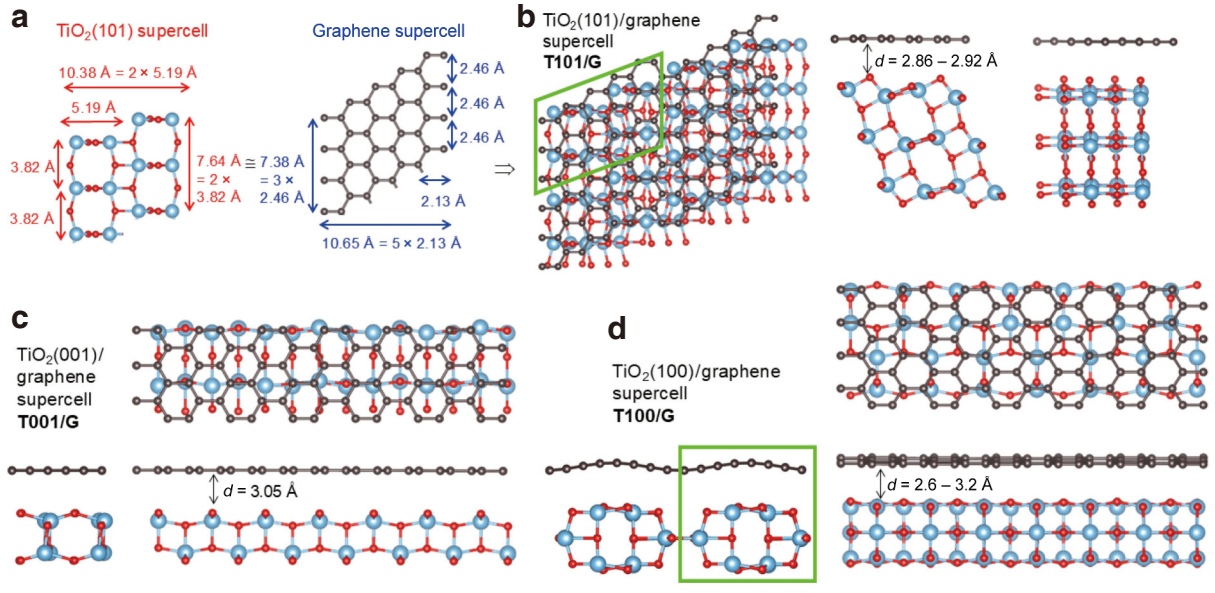

Fig. 1. Structures of TiO_2/graphene supercells. a, Construction of a commensurate TiO_2(101)/graphene supercell from TiO_2 and graphene supercells. **b–d,** Optimised geometries of commensurate supercells: b, TiO_2(101)/graphene; c, TiO_2(001)/graphene; d, TiO_2(100)/graphene. Top, front, and side views are shown for all TiO_2/graphene supercells. Distances from C atoms to the top layer of O atoms of TiO_2 are indicated. In this figure and the following figures, C atoms are shown in grey, C in red, and Ti in light blue. In the top view of the TiO_2(101)/graphene structure and in the front view of the TiO_2(100)/graphene structure, the supercell is indicated in green.

Table 1 Sizes of the commensurate TiO_2/graphene supercells used in this study: supercell dimensions, numbers of atoms, and strain on the graphene lattice. The table also presents shorthand notation used for TiO_2/graphene heterostructures in this manuscript

Interface		TiO_2(101)/graphene	TiO_2(001)/graphene	TiO_2(100)/graphene
Shorthand notation		T101/G	T001/G	T100/G
Extension of the graphene supercell		5 × 3	12 × 3	12 × 4
Extension of the TiO_2 supercell		2 × 2	7 × 2	7 × 1
Supercell dimensions (Å)		10.38 × 7.64	26.49 × 7.57	26.49 × 9.51
Number of repeat layers of TiO_2		3	2	3
Number of C atoms		30	72	96
Number of TiO_2 units		24	28	42
Total number of atoms		102	156	222
Strain on graphene (%)	in the *x* direction	−2.6	+3.6	+3.6
	in the *y* direction	+3.5	+2.6	−3.3

Anatase slabs with (001) and (100) crystallographic orientations required larger supercell extensions to achieve commensurability with graphene: 12 × 3 and 12 × 4 extensions of the graphene unit cell and 7 × 2 and 7 × 1 extensions of the anatase unit cells for the interfaces with anatase(001) and (100), respectively (structures T001/G and T100/G in Figs. 1c and 1d). Because of the large sizes of these supercells, we used thin TiO_2 slabs with two repeat layers for anatase(001) and three repeat layers for anatase(100). This slab thickness is sufficient for anatase(001) according to our earlier study of anatase crystallographic surfaces[62], while anatase(100) surface energies converge slowly with slab thickness, and a thicker slab may be needed to achieve fully converged surface properties[62]. We note that the anatase(101)/graphene supercell used in this study is the same as that in earlier studies[45, 47], while earlier studies of anatase(001)/graphene interfaces used different-shaped supercells with larger strain[38, 46, 50].

3.2 Binding at TiO_2/graphene interfaces

Geometry optimisations were carried out for the heterointerfaces of graphene with anatase(101), (001), and (100). As seen in the images of optimised structures in Figs. 1b–1d, no covalent bonds are formed at the TiO_2/graphene interfaces. Graphene layers are physisorbed at 2.6–3.2 Å above the top of the TiO_2 slabs, similar but slightly smaller distance than the 3.3 Å interlayer spacing in graphite. The presence of TiO_2 does have some effect on the graphene sheet: While graphene above the anatase(001) surface is completely flat (within 0.01 Å), graphene above the more corrugated anatase(101) surface is slightly non-planar (the *z*-coordinates of C atoms vary within 0.06 Å). By comparison, the (100) surface of anatase is more strongly corrugated, as seen in the expanded view in Fig. 1d; accordingly, noticeable curvature is seen in the graphene overlayer, with the *z*-coordinates of C atoms varying within 0.55 Å, in sync with the top regions and troughs of the anatase surface. To check whether this curvature is caused by the interaction with TiO_2 or is an artifact of the supercell size, we re-optimised the graphene sheet, starting from either flat graphene or graphene in the optimised TiO_2(100)/graphene interface, using the commensurate supercell size for this interface in both cases. In both cases, the optimised graphene sheet was non-planar with the *z*-coordinate variation up to 0.37 Å, which is less than the variation of up to 0.55 Å in the TiO_2(100)/graphene interface. Therefore, the observed non-planarity of graphene in this interface is caused by a combination of lattice constraints and interactions with TiO_2.

The binding energies of these interfaces are presented in **Table 2** and compared to the literature values for rutile TiO_2(110)/graphene (rutile(110)/graphene) and graphite interlayer binding. For a meaningful comparison between different systems, binding energies are scaled per unit area and per C atom. It can be seen that the energies per atom are very similar for all three studied anatase/graphene interfaces, indicating that the nature and strength of interaction are the same. Interestingly, the binding at these interfaces is stronger than at the rutile(110)/graphene interface in Ref.[48]; this difference can be attributed to the structure of the rutile(110) surface, where only the bridging oxygens of TiO_2 are close enough to interact with graphene. By comparison, the experimental value of the interlayer binding energy in graphite[63] is similar to this work's values for anatase/graphene interfaces. The slightly stronger binding at anatase/graphene interfaces compared to graphene may be attributed to stronger van der Waals interactions of the relatively large and polarisable Ti atoms. Overall, the interlayer distances and binding energies indicate physisorption in TiO_2/graphene interfaces, with no spontaneous formation of covalent interfacial bonds.

To verify whether the strength and nature of binding are affected by the position of the graphene overlayer above the TiO_2 surfaces, potential energy surfaces were calculated for graphene above anatase(101), (001), and (100). Graphene layers were uniformly displaced in the *x* and *y* directions in steps of 0.2 Å on a two-dimensional grid covering the full supercells, and the geometries were re-optimised. Lateral positions of these displaced graphene

Table 2 Binding energies of TiO_2/graphene heterointerfaces: defect-free interfaces T101/G, T001/G, and T100/G, and the corresponding interfaces containing a carbon vacancy (denoted "v"); the later interfaces are either physisorbed ("p") or chemisorbed ("c1"–"c3"). All binding energies in this work were calculated using PBE + D3 method. Literature values of binding energies for rutile TiO_2(110)/graphene (theoretical) and graphite (experimental) are included

Structure	Interfacial bonding	Binding energies		
		per supercell (eV)	per C atom (eV/atom)	per unit area (J/m^2)
T101/G	Physisorption	−1.37	−0.046	−0.28
T001/G	Physisorption	−3.17	−0.044	−0.25
T100/G	Physisorption	−4.56	−0.047	−0.29
Rutile(110)/graphene (PBE + D2, Ref.[48])	Physisorption	−1.67	−0.023	−0.14
Graphite (experiment Ref.[63])	Physisorption	N/A	−0.035	−0.21
T101/Gv-p	Physisorption	−1.31	—	—
T101/Gv-c1	C–O, C–Ti	−1.21	—	—
T101/Gv-c2	C–O	−2.37	—	—
T001/Gv-p	Physisorption	−3.39	—	—
T001/Gv-c1	C–O, C–Ti	−4.29	—	—
T001/Gv-c2	C–O	−3.77	—	—
T100/Gv-p	Physisorption	−4.75	—	—
T100/Gv-c1	C–Ti	−4.42	—	—
T100/Gv-c2	C–O, C–Ti	−3.94	—	—
T100/Gv-c3	C–O	−5.30	—	—

layers did not change significantly during optimisation. The potential energy surfaces were very flat for all three interfaces, with variations in the binding energies up to 0.004, 0.16, and 0.04 eV for the interfaces with anatase(101), (001), and (100), respectively. Thus, only anatase(001) shows weak preference for specific positions of graphene overlayers, likely because of the favourable directional overlap of the surface oxygens' lone pairs with graphene's π-system. However, the nature of the binding at the interfaces remains unchanged, with no transition from physisorption to chemisorption.

To investigate the effect of the vertical position of graphene in the corrugated TiO_2(100)/graphene interface, we also calculated three alternative constrained versions of this interface, with graphene fixed to be planar at three different heights above TiO_2: (i) at the highest *z*-coordinates of graphene in the fully optimised interface (3.16 Å above the top of TiO_2), (ii) at the mean value of graphene *z*-coordinates (2.91 Å above TiO_2), and (iii) at the lowest graphene *z*-coordinates (2.66 Å above TiO_2). The binding energies in these interfaces were −4.19, −4.10, and −3.29 eV per supercell, respectively, indicating weaker binding compared to the fully optimised interface (−4.56 eV). Notably, the lowest considered height of graphene above TiO_2 had the least favourable binding, indicating significant repulsion. These results confirm that the rippling of graphene in the fully optimised interface helps achieve optimal interaction with TiO_2, which is particularly important for the strongly corrugated TiO_2(100) surface.

Since the aim of this study was to explore the possibility of formation of Ti–C or Ti–O–C interfacial bonds, we attempted to enforce the formation of interfacial bonds by reducing the distance between the graphene layer and the anatase surfaces to 2 Å. This approach mimics the local high-pressure environment that occurs in the ultrasonic treatment which is often used in the solvothermal synthesis of TiO_2/graphene composites[31, 38], or in mechanical mixing procedures, such as ball milling[64, 65]. However, such interfaces turned out to be strongly repulsive, and during optimization graphene returned to the optimal height of approximately 3.0 Å above the anatase surfaces. These results suggest that formation of chemical bonds at pure graphene/TiO_2 interfaces is unlikely. Therefore Ti–C and Ti–O–C bonds observed experimentally in TiO_2/graphene photocatalytic composites must originate from structures more chemically complex than pure graphene and pure TiO_2.

Both graphene and TiO_2 are known to contain defects. In particular, anatase can contain oxygen vacancies; however, vacancies in (101) and (001)-oriented anatase slabs are known to prefer subsurface positions[66, 67] and therefore are unlikely to affect interfacial bonding. Graphene can also contain carbon vacancies, e.g., carbon monovacancies where the removal of a carbon atom leaves three undercoordinated atoms surrounding the monovacancy site. The monovacancy in graphene can reconstruct through symmetry-breaking distortion, so that two undercoordinated carbon atoms form a new C–C bond, while the third carbon atom is lifted slightly out of the plane of the graphene sheet[68, 69]. Vacancies are often introduced during synthesis processes, for example, in synthesis of graphene by reduction of graphene oxide[70]. Therefore, we considered vacancy-containing graphene as a candidate material for interfacial chemical bond formation.

Defect-free anatase/graphene structures obtained in potential energy surface explorations were used as starting points for carbon vacancy-containing structures. For each of the T101/G, T001/G, and T100/G interfaces, we chose three structures with C atoms positioned directly above Ti atoms and/or O atoms of TiO_2. A carbon atom next to these carbons (not directly above O or Ti) was removed, thus creating a carbon vacancy, and the structures were optimised. Geometry optimisations of vacancy-containing interfaces resulted in physisorbed structures with no covalent bonds formed between C and Ti or O, as seen in **Fig. 2** (representative

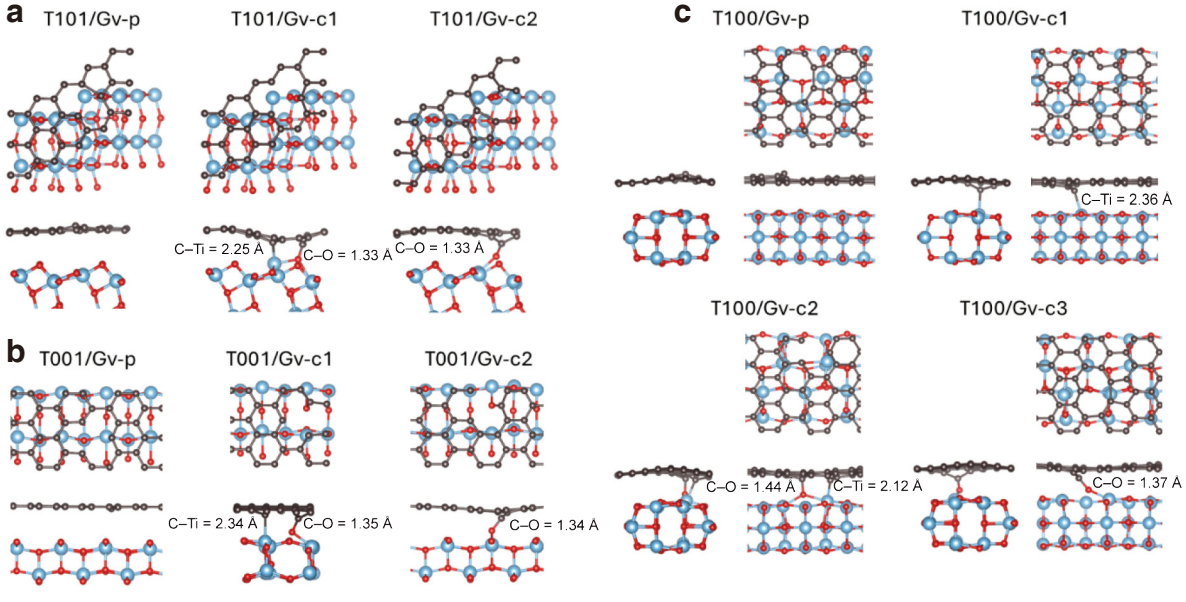

Fig. 2. Structures of TiO_2 with graphene containing carbon vacancies: a, TiO_2(101)/graphene, **b,** TiO_2(001)/graphene, **c,** TiO_2(100)/graphene. Cropped images are shown, showing only the interfacial regions for physisorbed structures, and only the regions around covalent interfacial bonds for chemisorbed structures. Top and side views are shown for TiO_2(101)/graphene and TiO_2(001)/graphene interfaces; and top, front, and side views for TiO_2(100)/graphene interfaces. Interfacial C–O and C–Ti covalent bond lengths are indicated.

structures T101/Gv-p, T001/Gv-p, and T100/Gv-p). The only exception is structure T100/Gv-c1, where a C atom near the vacancy site moved downwards and formed a 2.36 Å bond with a Ti atom. The binding energies of these vacancy-containing interfaces (Table 2) are within 0.2 eV of the corresponding defect-free interfaces. The similarities in the energies confirm that the nature of binding is the same, and the presence of undercoordinated carbon atoms at carbon vacancy sites does not significantly strengthen the binding.

To verify whether covalent interfacial bonds can form in defect-containing interfaces, graphene sheets with vacancy were then moved 1.5 Å down towards the anatase surfaces, similar to the approach described above for pristine graphene. A variety of outcomes were observed upon optimization: While some of these structures reverted to physisorbed interfaces, several structures formed covalent C–O and C–Ti interfacial bonds, as shown in Fig. 2 (structures T101/Gv-c1 and T101/Gv-c2, T001/Gv-c1 and T001/Gv-c2, and T100/Gv-c2 and T100/Gv-c3). Some of these covalently bonded interfaces were up to 1 eV more strongly bound than the corresponding physisorbed interfaces (Table 2). However, other covalently bonded structures were up to 0.8 eV less stable, suggesting that deformation of the graphene layer, as seen in Fig. 2, has a major effect on the stabilities of the interfaces. The binding energies showed no clear preference towards C–O bonded or combined C–Ti and C–O bonded interfaces. However, the T100/Gv-c1 structure bonded through a single Ti–C bond was less stable than the C–O bonded and physisorbed alternatives, suggesting that C–O bonds are more effective than Ti–C at stabilising TiO_2/graphene interfaces. This is consistent with experimental XPS studies of TiO_2/graphene photocatalysts typically reporting larger peaks for Ti–O–C bonds than for Ti–C bonds[31, 32, 34], and with some XPS studies reporting evidence of Ti–O–C bonds but no Ti–C bonds[39–41]. Interestingly, a study by Liu et al. comparing covalent bond formation at different TiO_2 crystal facets found Ti–O–C bonds formed at (101) and (001) facets and Ti–C bonds at (001) facets[24]. While our calculations found Ti–O–C bonds formed at all anatase facets, the (001) facet was the only one that spontaneously formed a Ti–C bond at the interface with vacancy-containing graphene.

In summary, our results suggest that all anatase surfaces can form covalent interfacial bonds with graphene, if the interfaces are subjected to high-pressure conditions and if defects (carbon vacancies) are present in the graphene layer. Both defects and high-pressure conditions can realistically occur in the synthesis of TiO_2/graphene composites: Graphene synthesised by reduction of graphene oxide was found to contain vacancies in concentrations up to 5%, depending on the method of reduction[70]. Synthetic techniques such as ball milling or ultrasonication used in solvothermal synthesis create local high-pressure environments; in particular, the pressure caused by ultrasonic treatment was reported to be large enough to cause C–C bond breaking at the interface with TiO_2[71]. We conclude that such conditions are likely to result in the formation of covalent bonds at TiO_2/graphene interfaces. It should be noted that vacancies in graphene are highly reactive: Earlier theoretical studies showed that graphene monovacancies readily react with oxygen and water molecules present in the ambient environment[72–76], and these molecules can form covalent bonds to the undercoordinated carbon atoms at the vacancy site, making these carbon atoms unavailable for covalent bonding to TiO_2. However, although dissociative adsorption of these molecules at graphene vacancies is favourable, the activation barriers were found to be high: 0.71–1.54 eV for dissociative adsorption of water[74, 76] and 5.25 eV for dissociative adsorption of O_2 at the graphene monovacancy[73]. Therefore some of the vacancies are likely to remain unpassivated, consistent with experimental observations of low concentrations of vacancies present in reduced graphene oxide[70]. Because of the low concentration of vacancies in graphene and the need for high-pressure environments, the number of interfacial Ti–C or Ti–O–C bonds is likely to be small, consistent with the small peaks for these bonds in XPS C 1s spectra[24, 31, 32, 34].

3.3 Electronic properties of TiO_2/graphene heterostructures

To understand the effect of interfacial binding on the electronic properties of TiO_2/graphene interfaces, we analysed band structures, densities of states, and charge density differences for all interfaces described in the previous section. Band structure plots for defect-free TiO_2/graphene interfaces in **Fig. 3** show that energy bands of these physisorbed systems are unchanged compared to isolated graphene sheets and isolated TiO_2 slabs. The differences in the band lines for the three TiO_2/graphene systems are caused by different sizes and shapes of the supercells, and therefore different shapes of the first Brillouin zone. Fig. 3 shows that graphene in the T001/G and T100/G interfaces remains semimetallic. The Dirac point of graphene in these systems is slightly above the Fermi level of the heterostructures, indicating that graphene behaves as electron donor. Interestingly, a small gap of 0.42 eV opens between the Y and Γ points in the band structure of graphene in the T101/G system. This small gap is also seen in the band structure of the isolated graphene sheet, therefore it is not caused by the formation of the physisorbed interface. It is unlikely to be caused by insufficient *k*-point sampling or by missing the Dirac point[77, 78], because a small gap is also visible in the density of states (Supplementary Fig. S1) calculated on a dense 12 × 12 × 1 *k*-point grid, and is still present when the density of the *k*-pint grid is increased to 24 × 24 × 1. The likely explanation is that the band gap opening is caused by the strain on the graphene lattice in the heterostructure. While previous studies showed that small uniaxial and isotropic biaxial strain do not open a band gap in graphene[48, 78–80], the anisotropic biaxial strain was shown to open a gap[79, 80]. In the parallelogram-shaped cell in T101/G, the application of biaxial strain in the *x* and *y* directions results in a loss of symmetry of graphene. A similar small gap was reported in an earlier study for the same T101/G interface[47]. Similarly, the gap opening was observed experimentally in graphene on SiC and attributed to the loss of symmetry in graphene[81]. However, experimentally synthesised TiO_2/graphene composites do not have the requirement to be commensurate, therefore the gap opening is likely to be an artifact of the commensurate cell in our computational model. Therefore, band structure data suggest that electronic properties of physisorbed TiO_2/graphene systems can be seen as simple superposition of the isolated TiO_2 and graphene components, without the formation of hybridised states.

The lack of coupling between TiO_2 and graphene states in the defect-free interfaces is supported by projected density of states (DOS) plots (Supplementary Fig. S1), which show that the states in the TiO_2 band gap (between −2 and +2 eV) are dominated by graphene, while the states in the TiO_2 valence and conduction band regions are dominated by O and Ti, respectively. Electron density

difference plots (Fig. 4) further confirm weak coupling in the physisorbed TiO_2/graphene systems: Very small charge transfer is observed from graphene to TiO_2, alongside noticeable charge rearrangement within the graphene sheet. In particular, in T100/G, where the TiO_2 surface is strongly corrugated, there is a transfer of charge within the graphene sheet towards carbon atoms that are directly above Ti and O atoms. Comparison with the constrained T100/G interfaces containing flat graphene (Supplementary Fig. S2) shows that the rippling and increased height of graphene above the highest region of the TiO_2(100) surface help avoid repulsion and ensure accumulation of electron density in the interfacial region, resulting in optimal binding.

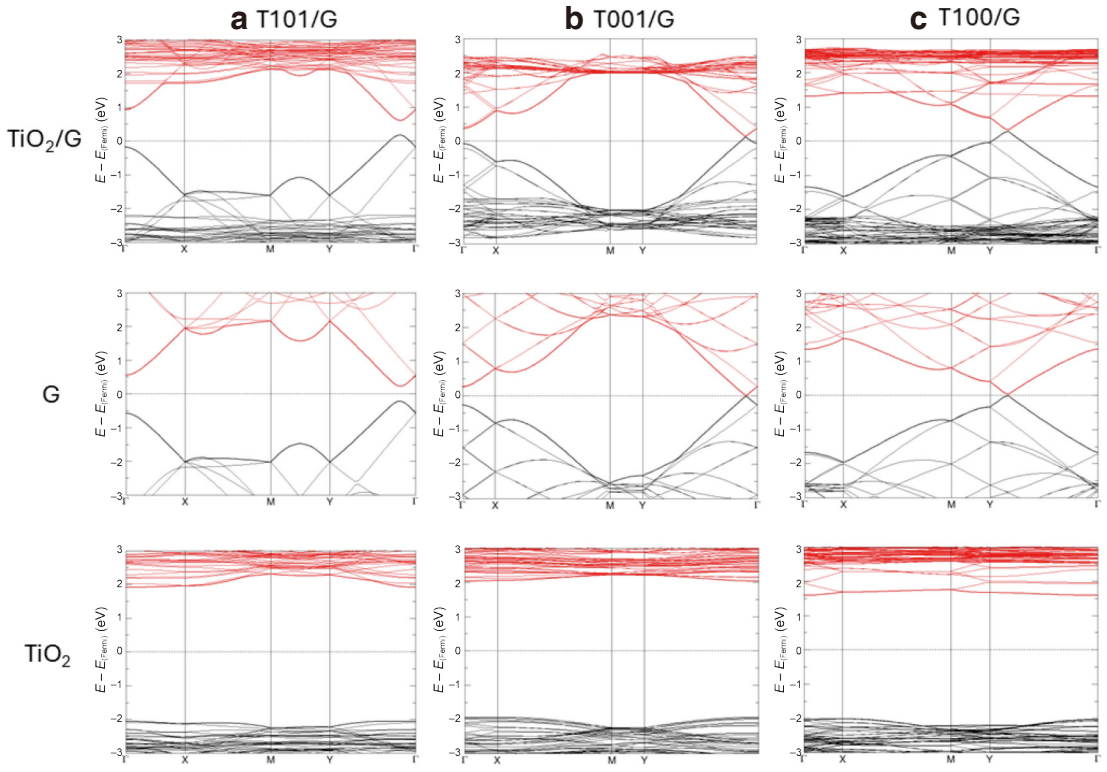

Fig. 3. Plots of band structures of defect-free TiO_2/graphene interfaces and isolated graphene and TiO_2 slabs along high-symmetry directions in the Brillouin zone. Top row: **a,** TiO_2(101)/graphene; **b,** TiO_2(001)/graphene; **c,** TiO_2(100)/graphene; Middle and bottom row: the corresponding isolated graphene and TiO_2 slabs, respectively. The isolated graphene and TiO_2 slabs have the same sizes and shapes as in the heterointerfaces. In all band structure plots, zero energy corresponds to the Fermi level; occupied levels are shown in black and unoccupied levels in red; the highest occupied and lowest unoccupied levels are shown as thicker lines; and the Fermi level is shown as a thin dashed line.

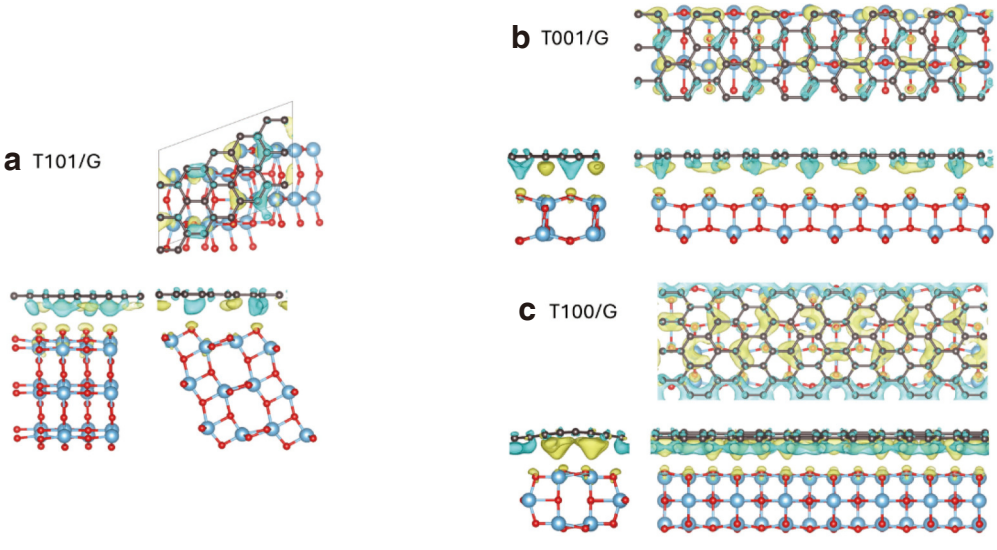

Fig. 4. Electron density differences in TiO_2/graphene defect-free interfaces: a, TiO_2(101)/graphene; **b,** TiO_2(001)/graphene; **c,** TiO_2(100)/graphene (top, front, and side views). Yellow corresponds to accumulation and cyan to depletion of electron density. Isosurfaces are drawn at +/−0.0005 electrons/Å^3.

Overall, the combination of band structure, density of states, and electron transfer data indicates that defect-free TiO_2/graphene interfaces interact via dispersion and charge transfer, without forming new hybrid electronic states. Since both TiO_2 and graphene states are present in the regions of TiO_2 valence and conduction band, such interfaces may facilitate transfer of photoexcited charges in TiO_2/graphene composites, but they are unlikely to achieve separation of charges or produce long-lived charges, since no trap states are formed.

TiO_2/graphene interfaces that contain carbon vacancies present a more complex picture. A monovacancy in graphene is known to give rise to strongly localised states above the Fermi level and a moderately localised state below the Fermi level[82]. Band structures presented in **Fig. 5**, and Supplementary Figs. S3 and S4 show that physisorbed TiO_2/graphene monovacancy systems retain these localised graphene monovacancy electronic states. Some of the weakly covalently bonded interfaces also retain the localised monovacancy states, for example, the T101/Gv-c1 interface bonded through C–Ti and C–O bonds (Supplementary Fig. S3c) and the T100/Gv-c1 interface bonded through a C–Ti bond (Supplementary Fig. S4c). Such localised states can act as electron or hole traps, which can be beneficial for photocatalytic systems, as they would prevent recombination of trapped electrons and holes. For example, an earlier theoretical study showed that electrons could be trapped at carbon vacancy sites at low temperatures, but escaped the defect site at room temperature[83]. Because of the small gap between the occupied and unoccupied trap states (ranging between 0.10 and 0.24 eV in the structures studied in this work), these trap states are unlikely to be effective in controlling the lifetimes of charge carriers in photocatalysis. Moreover, since these states are far from the reduction potentials of typical photocatalytic reactions, such as hydrogen reduction and water oxidation, the electrons and holes in these trap states would not be energetic enough to reduce or oxidise the species of interest in photocatalysis.

In contrast to physisorbed interfaces, the majority of the studied covalently bonded interfaces show changes in their band structures. For example, the lowest unoccupied state becomes delocalised and can no longer be described as a vacancy-based state in the T001/Gv-c2 system bonded through C–Ti and C–O bonds (Fig. 5d); both lowest unoccupied and the highest occupied states become delocalised in the T001/Gv-c1 system bonded through a C–O bond (Fig. 5c). Similar delocalisation effects are seen in heterostructures based on all studied TiO_2 surfaces. In the T101/Gv-c2 system bonded through a C–O bond, the highest occupied vacancy-based state moves up to the Fermi level, while the unoccupied state loses its localised character and overlaps in energy with TiO_2-based states (Supplementary Fig. S3d). In T100/Gv-c1 and T100/Gv-c2 systems (Supplementary Figs. S4d and S4e)), the lowest unoccupied states similarly lose their delocalised character. Therefore, it is clear that the covalent bonding between graphene and TiO_2 disrupts the carbon vacancy structure and affects the electronic properties of TiO_2/graphene heterostructures.

To get a better understanding of the nature of the interactions in covalently bonded TiO_2/graphene heterostructures, electron density difference plots of vacancy-containing interfaces were analysed. The plots in **Fig. 6a**, and Supplementary Figs. S5a and S6a for physisorbed heterostructures show rearrangements of electron density within graphene sheets, but no significant electron transfer

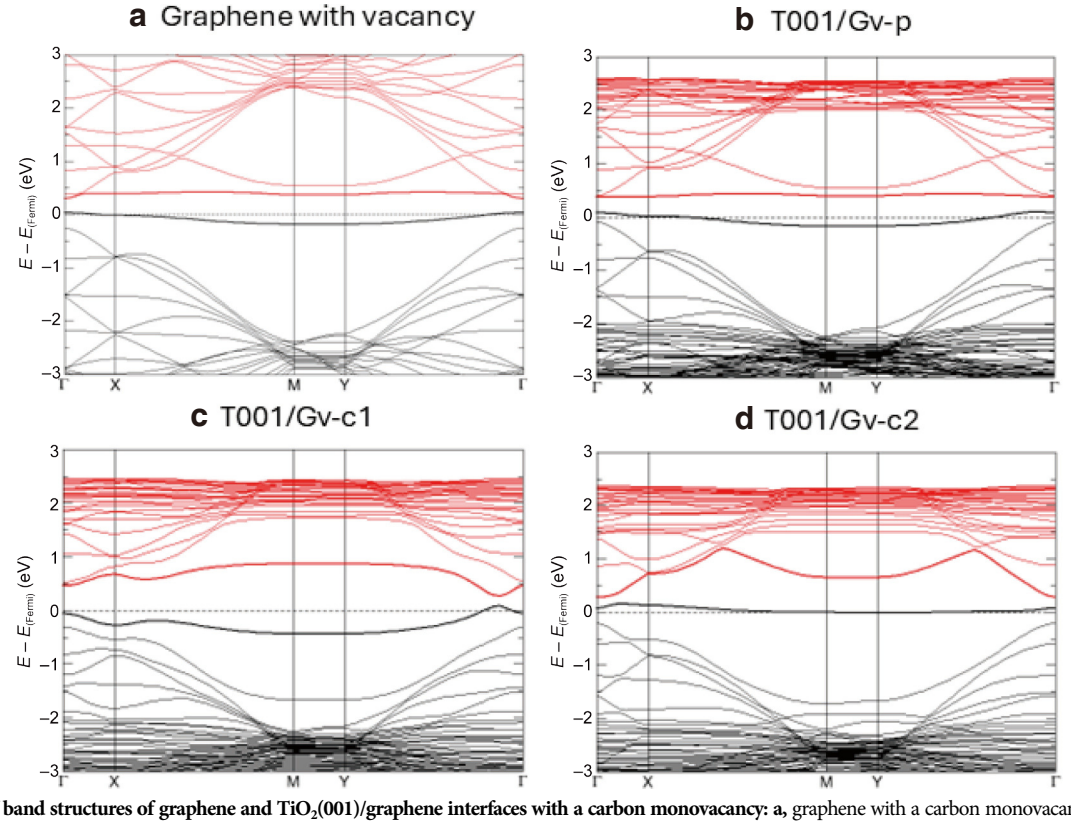

Fig. 5. Plots of band structures of graphene and TiO_2(001)/graphene interfaces with a carbon monovacancy: a, graphene with a carbon monovacancy, in a supercell used for TiO_2(001)/graphene interfaces; **b,** physisorbed TiO_2(001)/graphene monovacancy structure T001/Gv-p; **c,** chemisorbed TiO_2(001)/graphene monovacancy structure T001/Gv-c1 with a C–Ti and a C–O bond; **d,** chemisorbed TiO_2(001)/graphene monovacancy structure T001/Gv-c2 with a C–O bond.

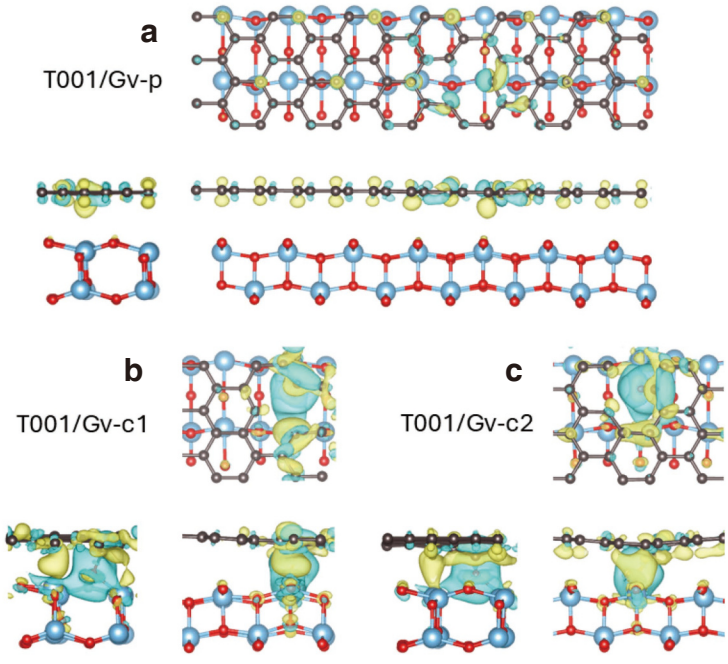

Fig. 6. Electron density differences in TiO_2(101)/graphene interfaces with carbon monovacancies: a, physisorbed interface; **b, c,** chemisorbed interfaces (top, front, and side views). Top and side views in (b and c) are truncated to show only the regions around the chemisorption site; no changes in electron density were visible far from the chemisorption site. Yellow corresponds to accumulation and cyan to depletion of electron density. Isosurfaces are drawn at +/−0.0025 electrons/Å^3.

between TiO_2 and graphene (note that the isosurfaces in Fig. 6, and Supplementary Figs. S5 and S6 are plotted at five times greater values compared to Fig. 4, to reflect larger electron density rearrangements around the vacancy site, therefore weak charge transfer to TiO_2 is not visible). In contrast, chemisorbed heterostructures show large complex rearrangements of electron density in the interface region, in particular, accumulation of electron density at the interfacial Ti–C bonds (structures T101/Gv-c1, T001/Gv-c1, and T100/Gv-c1) and at the oxygen atoms involved in the interfacial C–O bonds (all chemisorbed structures). This redistribution of electron density confirms the formation of covalent bonds at the interface and suggests that the altered electronic energy levels seen in the band structures of covalently bonded TiO_2/graphene heterointerfaces are likely to contain contributions of Ti and O as well as C atoms.

To understand the nature of the electronic states, densities of electronic states were plotted for all vacancy-containing heterostructures (**Fig. 7**, and Supplementary Figs. S7 and S8). In particular, densities of electronic states projected on the C, O, and Ti atoms at the vacancy sites and at covalent bonding sites were analysed. DOS plots of all physisorbed structures in Fig. 7a, and Supplementary Figs. S7a and S8a show sharp peaks above the Fermi level, consistent with the strongly localised bands discussed above. These sharp peaks are dominated by the three carbon atoms at the vacancy site (C1–C3). Other carbon atoms near the vacancy sites, such as C(gr1) in Fig. 7a, make much smaller contributions, while carbon atoms further away from the vacancy site, such as C(gr2) in the same figure, and all Ti and O atoms, make negligible contributions. The peaks below the Fermi level that correspond to the moderately localised highest occupied states are broader but are similarly dominated by carbon atoms near the vacancy site. There results confirm that there is little electronic coupling between graphene and TiO_2 states in physisorbed heterostructures, both with and without carbon vacancies.

By comparison, chemisorbed interfaces show evidence of electronic coupling between graphene and TiO_2. For example, the DOS of structure T001/Gv-c1 (Fig. 7b) shows a pair of states above and below the Fermi level, which correspond to the moderately localised states in the band structure plot in Fig. 5c. These peaks have obvious contributions of O and Ti; in particular, O1 strongly contributed to the occupied state and Ti1 to the unoccupied state. This suggests that these two states are somewhat spatially separated. This spatial separation can be expected to slow down recombination and give rise to longer-lived photoelectrons and photoholes.

Similarly, the highest occupied localised state near the Fermi level of structure T001/Gv-c2 in Fig. 7c has a strong contribution from O1, while the lowest unoccupied delocalised state is mainly carbon-based, but has some contributions from Ti1. The same behaviour is seen in interfaces based on TiO_2(101) and (100) surfaces: The states that were dominated by carbons at the vacancy sites in physisorbed heterostructures acquire non-negligible contributions of Ti and O in chemisorbed heterostructures. The extent of contributions of Ti and O atoms differs between structures and depends on the specific details of the interfacial bonding: In general, the structures that contain both C–Ti and C–O interfacial bonds show substantial contributions of both Ti and O in vacancy-based states (see structures T001/Gv-c1 in Fig. 7b, T101/Gv-c1 in Supplementary Fig. S7b, and T100/Gv-c2 in Supplementary Fig. S8c), while this effect is weaker in the structures that contain only either C–Ti or C–O interfacial bonds (structures T001/Gv-c2 in Fig. 7c, T101/Gv-c2 in Supplementary Fig. S7b, T100/Gv-c1 in Supplementary Fig. S8b, and T100/Gv-c3 in Supplementary Fig. S8d). At the same time, significant density of carbon electronic states can be seen alongside O and Ti states in the TiO_2 valence band edge (−2 eV) and conduction band edge (+1.5 eV) regions, especially in the T001/Gv-c1 interface in Fig. 7b and all T100/G interfaces (Supplementary Fig. S8). This suggests that graphene states are coupled with TiO_2

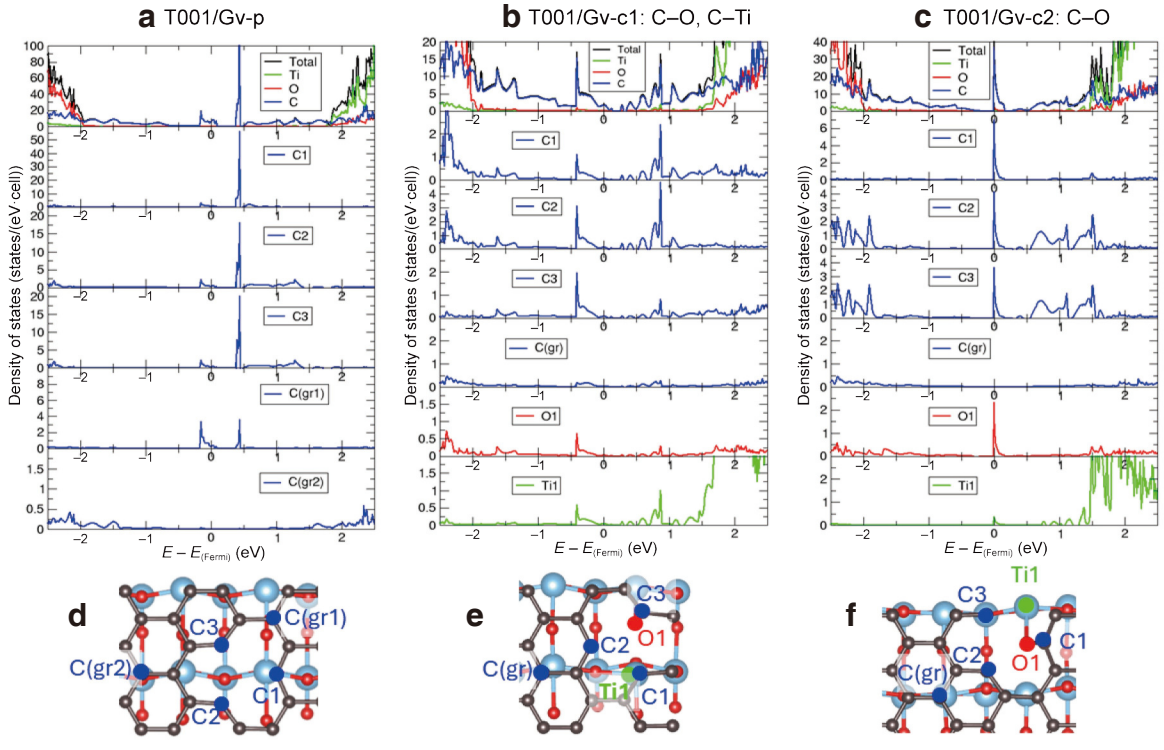

Fig. 7. Densities of electronic states and atomic structures of TiO_2(001)/graphene interfaces with a carbon vacancy. a–c, Total and projected densities of electronic states: a, T001/Gv-p physisorbed interface; b, T001/Gv-c1 chemisorbed interface bonded through C–Ti and C–O bonds; c, T001/Gv-c2 chemisorbed interface bonded through a C–O bond (c). **d–f,** Atomic structures for a–c. The top panels in a–c show the total contributions of Ti, O, and C atoms to the total DOS; while the lower panels show the contributions of individual atoms: C1–C3 are C atoms at the vacancy site; C(gr1) is a C atom near but near the vacancy site; C(gr) and C(gr2) are typical graphene carbon atoms away from the vacancy site; O1 is the O atom bonded to C1 (plots b and c); Ti1 is the Ti atom bonded to C2 (plot b) or to O1 (plot c where no C–Ti bonds are present). In panels d–f, the C atoms for the projected DOS plots are highlighted in blue, O atoms in red, and Ti atoms in green.

states not only in the band gap region but also in the TiO_2 valence and conduction band regions.

To assess the possibility of separation of photogenerated electrons and holes, exciton binding energies were calculated for the TiO_2/graphene interfaces and compared to exciton binding energies in pure TiO_2, as described in the Supporting Information (see Supplementary Table S1 and accompanying methodological details). Exciton binding energies in pure TiO_2 slabs were found to be surface-dependent and ranged between 60 and 112 meV, comparable to but slightly lower than literature values of around 200 meV[84, 85]. These values show that bound electron–hole pairs are stable in TiO_2 at room temperature. In contrast, exciton binding energies for the TiO_2/graphene interfaces were much smaller, between 0 and 10 meV, thanks to the high dispersion of the predominantly graphene-based valence and conduction band edge states. These values are well below the thermal energy of 26 meV, confirming that bound electron–hole pairs at these interfaces can easily dissociate at room temperature and avoid recombination.

Overall, these results show that covalent bonding at TiO_2/graphene interfaces significantly affects the electronic structure and gives rise to hybridised electronic states. This hybridisation of carbon and TiO_2 states, especially in the TiO_2 conduction band region, is significant for photocatalysis, because it can enable rapid transfer of photoelectrons between TiO_2 and graphene. The role of covalent interfacial bonds in facilitating photoelectron transfer from TiO_2 to graphene was postulated in experimental studies[24, 25, 32, 35, 38]. The hybridisation of C and Ti states seen in the projected DOS plots offers evidence that these covalent bonds provide a route for electron transfer between TiO_2 and graphene. Furthermore, the presence of hybridised highest occupied and lowest unoccupied states that are somewhat spatially separated is also beneficial for photocatalysis, because these states may act as electron and hole trap states. The partial spatial separation of these states is likely to slow down recombination of trapped electrons and holes and prolong the lifetimes of photoexcited charge carriers available for photocatalytic reactions[24, 25, 35].

4 Conclusions

In summary, we performed density functional theory studies of the nature of interfacial binding in heterostructures of graphene with anatase TiO_2. Our results show that pristine graphene interacts with (101), (001), and (100) surfaces of anatase by physisorption. However, if carbon vacancies are present in graphene and are not passivated by water or oxygen molecules, they can give rise to covalent bonding between graphene and anatase, forming interfacial C–O and C–Ti bonds. This covalent bonding affects electronic properties of TiO_2/graphene composites, creating hybridised states, and in particular giving rise to electron and hole trap states partially localised on the Ti and O atoms involved in the interfacial bonds. These partially localised trap states can prevent electron–hole recombination and therefore increase photocatalytic efficiency of covalently bonded TiO_2/graphene composites. By revealing the properties of carbon vacancy-related states at TiO_2/graphene interfaces, this study highlights the important role

played by interfacial defects in controlling the efficiency of photocatalytic heterostructures.

Since carbon vacancies are not the only defect that can exist in TiO_2/graphene systems, further studies could consider the effects of other defects, such as carbon interstitials in graphene and oxygen vacancies in TiO_2, to explore their role in interfacial binding and the effect on charge separation at these interfaces and to pinpoint the structures responsible for enhanced charge separation and high photocatalytic efficiency of TiO_2/graphene composites.

References

[1] Romero, E.; Novoderezhkin, V. I.; Van Grondelle, R. Quantum design of photosynthesis for bio-inspired solar-energy conversion. *Nature* **2017**, *543*, 355–365.

[2] Zhang, B. B.; Sun, L. C. Artificial photosynthesis: Opportunities and challenges of molecular catalysts. *Chem. Soc. Rev.* **2019**, *48*, 2216–2264.

[3] Lingampalli, S. R.; Ayyub, M. M.; Rao, C. N. R. Recent progress in the photocatalytic reduction of carbon dioxide. *ACS Omega* **2017**, *2*, 2740–2748.

[4] Ran, J. R.; Jaroniec, M.; Qiao, S. Z. Cocatalysts in semiconductor-based photocatalytic CO_2 reduction: Achievements, challenges, and opportunities. *Adv. Mater.* **2018**, *30*, 1704649.

[5] Fang, S. Y.; Rahaman, M.; Bharti, J.; Reisner, E.; Robert, M.; Ozin, G. A.; Hu, Y. H. Photocatalytic CO_2 reduction. *Nat. Rev. Methods Primers* **2023**, *3*, 61.

[6] Chen, X. B.; Shen, S. H.; Guo, L. J.; Mao, S. S. Semiconductor-based photocatalytic hydrogen generation. *Chem. Rev.* **2010**, *110*, 6503–6570.

[7] Corredor, J.; Rivero, M. J.; Rangel, C. M.; Gloaguen, F.; Ortiz, I. Comprehensive review and future perspectives on the photocatalytic hydrogen production. *J. Chem. Technol. Biotechnol.* **2019**, *94*, 3049–3063.

[8] Molaei, M. J. Recent advances in hydrogen production through photocatalytic water splitting: A review. *Fuel* **2024**, *365*, 131159.

[9] Ren, H. J.; Koshy, P.; Chen, W. F.; Qi, S. H.; Sorrell, C. C. Photocatalytic materials and technologies for air purification. *J. Hazard. Mater.* **2017**, *325*, 340–366.

[10] He, F.; Jeon, W.; Choi, W. Photocatalytic air purification mimicking the self-cleaning process of the atmosphere. *Nat. Commun.* **2021**, *12*, 2528.

[11] Mulay, M. R.; Martsinovich, N. TiO_2 photocatalysts for degradation of micropollutants in water. In *Clean Water and Sanitation*. Leal Filho, W.; Azul, A. M.; Brandli, L.; Lange Salvia, A.; Wall, T., Eds.; Springer: Cham, 2021; pp 1–19.

[12] Ren, G. M.; Han, H. T.; Wang, Y. X.; Liu, S. T.; Zhao, J. Y.; Meng, X. C.; Li, Z. Z. Recent advances of photocatalytic application in water treatment: A review. *Nanomaterials* **2021**, *11*, 1804.

[13] Fujishima, A.; Zhang, X. T.; Tryk, D. A. TiO_2 photocatalysis and related surface phenomena. *Surf. Sci. Rep.* **2008**, *63*, 515–582.

[14] Nakata, K.; Fujishima, A. TiO_2 photocatalysis: Design and applications. *J. Photochem. Photobiol. C: Photochem. Rev.* **2012**, *13*, 169–189.

[15] Lee, S. Y.; Park, S. J. TiO_2 photocatalyst for water treatment applications. *J. Ind. Eng. Chem.* **2013**, *19*, 1761–1769.

[16] Armaković, S. J.; Savanović, M. M.; Armaković, S. Titanium dioxide as the most used photocatalyst for water purification: An overview. *Catalysts* **2023**, *13*, 26.

[17] Henderson, M. A. A surface science perspective on TiO_2 photocatalysis. *Surf. Sci. Rep.* **2011**, *66*, 185–297.

[18] Pelaez, M.; Nolan, N. T.; Pillai, S. C.; Seery, M. K.; Falaras, P.; Kontos, A. G.; Dunlop, P. S. M.; Hamilton, J. W. J.; Byrne, J. A.; O'Shea, K. et al. A review on the visible light active titanium dioxide photocatalysts for environmental applications. *Appl. Catal. B: Environ.* **2012**, *125*, 331–349.

[19] Morales-Torres, S.; Pastrana-Martínez, L. M.; Figueiredo, J. L.; Faria, J. L.; Silva, A. M. T. Design of graphene-based TiO_2 photocatalysts—A review. *Environ. Sci. Pollut. Res. Int.* **2012**, *19*, 3676–3687.

[20] Padmanabhan, N. T.; Thomas, N.; Louis, J.; Mathew, D. T.; Ganguly, P.; John, H.; Pillai, S. C. Graphene coupled TiO_2 photocatalysts for environmental applications: A review. *Chemosphere* **2021**, *271*, 129506.

[21] Badoni, A.; Thakur, S.; Vijayan, N.; Swart, H. C.; Bechelany, M.; Chen, Z. S.; Sun, S. H.; Cai, Q. R.; Chen, Y.; Prakash, J. Recent progress in understanding the role of graphene oxide, TiO_2 and graphene oxide-TiO_2 nanocomposites as multidisciplinary photocatalysts in energy and environmental applications. *Catal. Sci. Technol.* **2025**, *15*, 1702–1770.

[22] Yang, Y. F.; Xu, L. D.; Wang, H. F.; Wang, W. J.; Zhang, L. X. TiO_2/graphene porous composite and its photocatalytic degradation of methylene blue. *Mater. Des.* **2016**, *108*, 632–639.

[23] Mehta, M.; Chandrabose, G.; Krishnamurthy, S.; Avasthi, D. K.; Chowdhury, S. Improved photoelectrochemical properties of TiO_2-graphene nanocomposites: Effect of defect induced visible light absorption and graphene conducting channel for carrier transport. *Appl. Surf. Sci. Adv.* **2022**, *11*, 100274.

[24] Liu, L. C.; Liu, Z.; Liu, A. N.; Gu, X. R.; Ge, C. Y.; Gao, F.; Dong, L. Engineering the TiO_2-graphene interface to enhance photocatalytic H_2 production. *ChemSusChem* **2014**, *7*, 618–626.

[25] Huang, Q. W.; Tian, S. Q.; Zeng, D. W.; Wang, X. X.; Song, W. L.; Li, Y. Y.; Xiao, W.; Xie, C. S. Enhanced photocatalytic activity of chemically bonded TiO_2/graphene composites based on the effective interfacial charge transfer through the C–Ti bond. *ACS Catal.* **2013**, *3*, 1477–1485.

[26] Zhang, Q. Z.; Bao, N.; Wang, X. Q.; Hu, X. D.; Miao, X. H.; Chaker, M.; Ma, D. L. Advanced fabrication of chemically bonded graphene/TiO_2 continuous fibers with enhanced broadband photocatalytic properties and involved mechanisms exploration. *Sci. Rep.* **2016**, *6*, 38066.

[27] Niu, X. Y.; Yu, J. Y.; Wang, L. K.; Fu, C.; Wang, J. X.; Wang, L.; Zhao, H. L.; Yang, J. K. Enhanced photocatalytic performance of TiO_2 nanotube based heterojunction photocatalyst via the coupling of graphene and FTO. *Appl. Surf. Sci.* **2017**, *413*, 7–15.

[28] Liu, G. Y.; Li, K. K.; Jia, J.; Zhang, Y. T. Coal-based graphene as a promoter of TiO_2 catalytic activity for the photocatalytic degradation of organic dyes. *New Carbon Mater.* **2022**, *37*, 1172–1180.

[29] Min, Y. L.; Zhang, K.; Zhao, W.; Zheng, F. C.; Chen, Y. C.; Zhang, Y. G. Enhanced chemical interaction between TiO_2 and graphene oxide for photocatalytic decolorization of methylene blue. *Chem. Eng. J.* **2012**, *193–194*, 203–210.

[30] Umrao, S.; Abraham, S.; Theil, F.; Pandey, S.; Ciobota, V.; Shukla, P. K.; Rupp, C. J.; Chakraborty, S.; Ahuja, R.; Popp, J. et al. A possible mechanism for the emergence of an additional band gap due to a Ti–O–C bond in the TiO_2-graphene hybrid system for enhanced photodegradation of methylene blue under visible light. *RSC Adv.* **2014**, *4*, 59890–59901.

[31] Pei, F. Y.; Xu, S. G.; Zuo, W.; Zhang, Z. R.; Liu, Y. L.; Cao, S. K. Effective improvement of photocatalytic hydrogen evolution via a facile *in-situ* solvothermal N-doping strategy in N-TiO_2/N-graphene nanocomposite. *Int. J. Hydrogen Energy* **2014**, *39*, 6845–6852.

[32] Bhirud, A. P.; Sathaye, S. D.; Waichal, R. P.; Ambekar, J. D.; Park, C. J.; Kale, B. B. *In-situ* preparation of N-TiO_2/graphene nanocomposite and its enhanced photocatalytic hydrogen production by H_2S splitting under solar light. *Nanoscale* **2015**, *7*, 5023–5034.

[33] Qiu, B. C.; Zhou, Y.; Ma, Y. F.; Yang, X. L.; Sheng, W. Q.; Xing, M. Y.; Zhang, J. L. Facile synthesis of the Ti^{3+} self-doped TiO_2-graphene nanosheet composites with enhanced photocatalysis. *Sci. Rep.* **2015**, *5*, 8591.

[34] Zhang, Y.; Li, L. D.; Liu, H. Y.; Lu, T. S. Graphene oxide and F co-doped TiO_2 with (001) facets for the photocatalytic reduction of

bromate: Synthesis, characterization and reactivity. *Chem. Eng. J.* **2017**, *307*, 860–867.

[35] Wang, S. L.; Li, J.; Wang, S. J.; Wu, J. E.; Wong, T. I.; Foo, M. L.; Chen, W.; Wu, K.; Xu, G. Q. Two-dimensional C/TiO_2 heterogeneous hybrid for noble-metal-free hydrogen evolution. *ACS Catal.* **2017**, *7*, 6892–6900.

[36] Lu, D. Z.; Yang, M. C.; Wang, H. M.; Kumar, K. K.; Wu, P.; D, N. *In situ* hydrothermal synthesis of Y-TiO_2/graphene heterojunctions with improved visible-light-driven photocatalytic properties. *Ceram. Int.* **2017**, *43*, 16753–16762.

[37] Yu, W. B.; Zhang, H. R.; Zhang, H. W.; Liu, Y.; Li, Y.; Su, B. L. Modulating Ti T_{2g} orbital bonding in dual-channeled TiO_2/rGO hybrid architecture for stable photocatalytic methanol to hydrogen. *Adv. Funct. Mater.* **2024**, *34*, 2410816.

[38] Yang, N. L.; Liu, Y. Y.; Wen, H.; Tang, Z. Y.; Zhao, H. J.; Li, Y. L.; Wang, D. Photocatalytic properties of graphdiyne and graphene modified TiO_2: From theory to experiment. *ACS Nano* **2013**, *7*, 1504–1512.

[39] Žerjav, G.; Arshad, M. S.; Djinović, P.; Junkar, I.; Kovač, J.; Zavašnik, J.; Pintar, A. Improved electron–hole separation and migration in anatase TiO_2 nanorod/reduced graphene oxide composites and their influence on photocatalytic performance. *Nanoscale* **2017**, *9*, 4578–4592.

[40] Khan, M. A. M.; Ansari, A. A.; Choudhary, P.; Ahmed, J.; Kumar, S.; Hussain, S. Reduced graphene oxide supported Ag-loaded brookite TiO_2 nanowires: Enhanced photocatalytic degradation performance and electrochemical energy storage applications. *Diamond Relat. Mater.* **2023**, *139*, 110397.

[41] Huynh, T. P.; Do, T. C. M. V.; Le, P. H. TiO_2 nanotube arrays decorated with graphene/graphite oxide nanocomposite for the photocatalytic degradation of anticancer drugs in the aquatic environment. *ACS Appl. Nano Mater.* **2024**, *7*, 20012–20023.

[42] Sumerel, J. L.; Yang, W. J.; Kisailus, D.; Weaver, J. C.; Choi, J. H.; Morse, D. E. Biocatalytically templated synthesis of titanium dioxide. *Chem. Mater.* **2003**, *15*, 4804–4809.

[43] Ayissi, S.; Charpentier, P. A.; Farhangi, N.; Wood, J. A.; Palotás, K.; Hofer, W. A. Interaction of titanium oxide nanostructures with graphene and functionalized graphene nanoribbons: A DFT study. *J. Phys. Chem. C* **2013**, *117*, 25424–25432.

[44] Bukowski, B.; Deskins, N. A. The interactions between TiO_2 and graphene with surface inhomogeneity determined using density functional theory. *Phys. Chem. Chem. Phys.* **2015**, *17*, 29734–29746.

[45] Li, X. H.; Gao, H. T.; Liu, G. J. A LDA+*U* study of the hybrid graphene/anatase TiO_2 nanocomposites: Interfacial properties and visible light response. *Comput. Theor. Chem.* **2013**, *1025*, 30–34.

[46] Masuda, Y.; Giorgi, G.; Yamashita, K. DFT study of anatase-derived TiO_2 nanosheets/graphene hybrid materials. *Phys. Status Solidi (B)* **2014**, *251*, 1471–1479.

[47] Ferrighi, L.; Fazio, G.; di Valentin, C. Charge carriers separation at the graphene/(101) anatase TiO_2 interface. *Adv. Mater. Interfaces* **2016**, *3*, 1500624.

[48] Gillespie, P. N. O.; Martsinovich, N. Electronic structure and charge transfer in the TiO_2 rutile (110)/graphene composite using hybrid DFT calculations. *J. Phys. Chem. C* **2017**, *121*, 4158–4171.

[49] Martins, P. M.; Ferreira, C. G.; Silva, A. R.; Magalhães, B.; Alves, M. M.; Pereira, L.; Marques, P. A. A. P.; Melle-Franco, M.; Lanceros-Méndez, S. TiO_2/graphene and TiO_2/graphene oxide nanocomposites for photocatalytic applications: A computer modeling and experimental study. *Compos. Part B: Eng.* **2018**, *145*, 39–46.

[50] Mishra, S. B.; Roy, S. C.; Nanda, B. R. K. Electronic structure of graphene/TiO_2 interface: Design and functional perspectives. *Appl. Surf. Sci.* **2021**, *542*, 148709.

[51] Gillespie, P. N. O.; Martsinovich, N. Origin of charge trapping in TiO_2/reduced graphene oxide photocatalytic composites: Insights from theory. *ACS Appl. Mater. Interfaces* **2019**, *11*, 31909–31922.

[52] Kühne, T. D.; Iannuzzi, M.; Del Ben, M.; Rybkin, V. V.; Seewald, P.; Stein, F.; Laino, T.; Khaliullin, R. Z.; Schütt, O.; Schiffmann, F. et al. CP2K: An electronic structure and molecular dynamics software package—Quickstep: Efficient and accurate electronic structure calculations. *J. Chem. Phys.* **2020**, *152*, 194103.

[53] Perdew, J. P.; Burke, K.; Ernzerhof, M. Generalized gradient approximation made simple. *Phys. Rev. Lett.* **1996**, *77*, 3865–3868.

[54] Grimme, S.; Ehrlich, S.; Goerigk, L. Effect of the damping function in dispersion corrected density functional theory. *J. Comput. Chem.* **2011**, *32*, 1456–1465.

[55] Goedecker, S.; Teter, M.; Hutter, J. Separable dual-space Gaussian pseudopotentials. *Phys. Rev. B* **1996**, *54*, 1703–1710.

[56] Boys, S. F.; Bernardi, F. The calculation of small molecular interactions by the differences of separate total energies. Some procedures with reduced errors. *Mol. Phys.* **1970**, *19*, 553–566.

[57] Dovesi, R.; Erba, A.; Orlando, R.; Zicovich-Wilson, C. M.; Civalleri, B.; Maschio, L.; Rérat, M.; Casassa, S.; Baima, J.; Salustro, S. et al. Quantum-mechanical condensed matter simulations with CRYSTAL. *WIREs Comput. Mol. Sci.* **2018**, *8*, e1360.

[58] Heyd, J.; Scuseria, G. E.; Ernzerhof, M. Hybrid functionals based on a screened Coulomb potential. *J. Chem. Phys.* **2003**, *118*, 8207–8215.

[59] Heyd, J.; Scuseria, G. E.; Ernzerhof, M. Erratum: "Hybrid functionals based on a screened Coulomb potential". *J. Chem. Phys.* **2006**, *124*, 219906.

[60] Grimme, S. Semiempirical GGA-type density functional constructed with a long-range dispersion correction. *J. Comput. Chem.* **2006**, *27*, 1787–1799.

[61] Wen, C. Z.; Jiang, H. B.; Qiao, S. Z.; Yang, H. G.; Lu, G. Q. Synthesis of high-reactive facets dominated anatase TiO_2. *J. Mater. Chem.* **2011**, *21*, 7052–7061.

[62] Martsinovich, N.; Troisi, A. How TiO_2 crystallographic surfaces influence charge injection rates from a chemisorbed dye sensitiser. *Phys. Chem. Chem. Phys.* **2012**, *14*, 13392–13401.

[63] Benedict, L. X.; Chopra, N. G.; Cohen, M. L.; Zettl, A.; Louie, S. G.; Crespi, V. H. Microscopic determination of the interlayer binding energy in graphite. *Chem. Phys. Lett.* **1998**, *286*, 490–496.

[64] Ahmad, J.; Sofi, F. A.; Mehraj, O.; Majid, K. Fabrication of highly photocatalytic active anatase TiO_2-graphene oxide heterostructures via solid phase ball milling for environmental remediation. *Surf. Interfaces* **2018**, *13*, 186–195.

[65] Sidoli, M.; Magnani, G.; Fornasini, L.; Scaravonati, S.; Morenghi, A.; Vezzoni, V.; Bersani, D.; Bertoni, G.; Gaboardi, M.; Riccò, M. et al. Defective graphene decorated with TiO_2 nanoparticles as negative electrode in Li-ion batteries. *J. Alloys Compd.* **2023**, *958*, 170420.

[66] Cheng, H. Z.; Selloni, A. Energetics and diffusion of intrinsic surface and subsurface defects on anatase TiO_2(101). *J. Chem. Phys.* **2009**, *131*, 054703.

[67] Cheng, H. Z.; Selloni, A. Surface and subsurface oxygen vacancies in anatase TiO_2 and differences with rutile. *Phys. Rev. B* **2009**, *79*, 092101.

[68] El-Barbary, A. A.; Telling, R. H.; Ewels, C. P.; Heggie, M. I.; Briddon, P. R. Structure and energetics of the vacancy in graphite. *Phys. Rev. B* **2003**, *68*, 144107.

[69] Robertson, A. W.; Montanari, B.; He, K.; Allen, C. S.; Wu, Y. A.; Harrison, N. M.; Kirkland, A. I.; Warner, J. H. Structural reconstruction of the graphene monovacancy. *ACS Nano* **2013**, *7*, 4495–4502.

[70] Lesiak, B.; Trykowski, G.; Tóth, J.; Biniak, S.; Kövér, L.; Rangam, N.; Stobinski, L.; Malolepszy, A. Chemical and structural properties of reduced graphene oxide-dependence on the reducing agent. *J. Mater. Sci.* **2021**, *56*, 3738–3754.

[71] Xing, M. Y.; Shen, F.; Qiu, B. C.; Zhang, J. L. Highly-dispersed boron-doped graphene nanosheets loaded with TiO_2 nanoparticles for enhancing CO_2 photoreduction. *Sci. Rep.* **2014**, *4*, 6341.

[72] Qi, X. J.; Guo, X.; Zheng, C. G. Density functional study the interaction of oxygen molecule with defect sites of graphene. *Appl. Surf. Sci.* **2012**, *259*, 195–200.

[73] Xu, Z. M.; Ao, Z. M.; Chu, D. W.; Younis, A.; Li, C. M.; Li, S. A. Reversible hydrophobic to hydrophilic transition in graphene via water splitting induced by UV irradiation. *Sci. Rep.* **2014**, *4*, 6450.
[74] Błoński, P.; Otyepka, M. First-principles study of the mechanism of wettability transition of defective graphene. *Nanotechnology* **2017**, *28*, 064003.
[75] Datteo, M.; Liu, H. S.; Di Valentin, C. Water on graphene-coated TiO_2: Role of atomic vacancies. *ACS Appl. Mater. Interfaces* **2018**, *10*, 5793–5804.
[76] Pozzo, M.; Lacovig, P.; Bianchi, M.; Schied, M.; Bignardi, L.; Zarotti, F.; Felici, R.; Alfè, D.; Lizzit, S.; Larciprete, R. Room temperature water splitting at the basal plane of graphene grown on nickel. *Carbon* **2025**, *243*, 120422.
[77] Farjam, M.; Rafii-Tabar, H. Comment on "Band structure engineering of graphene by strain: First-principles calculations". *Phys. Rev. B* **2009**, *80*, 167401.
[78] Gui, G.; Li, J.; Zhong, J. X. Reply to "Comment on "Band structure engineering of graphene by strain: First-principles calculations"" *Phys. Rev. B* **2009**, *80*, 167402.
[79] Cocco, G.; Cadelano, E.; Colombo, L. Gap opening in graphene by shear strain. *Phys. Rev. B* **2010**, *81*, 241412(R).
[80] Kerszberg, N.; Suryanarayana, P. *Ab initio* strain engineering of graphene: Opening bandgaps up to 1 eV. *RSC Adv.* **2015**, *5*, 43810–43814.
[81] Zhou, S. Y.; Gweon, G. H.; Fedorov, A. V.; First, P. N.; de Heer, W. A.; Lee, D. H.; Guinea, F.; Castro Neto, A. H.; Lanzara, A. Substrate-induced bandgap opening in epitaxial graphene. *Nat. Mater.* **2007**, *6*, 770–775.
[82] Amara, H.; Latil, S.; Meunier, V.; Lambin, P.; Charlier, J. C. Scanning tunneling microscopy fingerprints of point defects in graphene: A theoretical prediction. *Phys. Rev. B* **2007**, *76*, 115423.
[83] Tachikawa, H.; Kawabata, H. Electronic states of defect sites of graphene model compounds: A DFT and direct molecular orbital-molecular dynamics study. *J. Phys. Chem. C* **2009**, *113*, 7603–7609.
[84] Baldini, E.; Chiodo, L.; Dominguez, A.; Palummo, M.; Moser, S.; Yazdi-Rizi, M.; Auböck, G.; Mallett, B. P. P.; Berger, H.; Magrez, A. et al. Strongly bound excitons in anatase TiO_2 single crystals and nanoparticles. *Nat. Commun.* **2017**, *8*, 13.
[85] Wang, A. L.; Jiang, X.; Zheng, Q. J.; Petek, H.; Zhao, J. Ultrafast many-body bright-dark exciton transition in anatase TiO_2. *Proc. Natl. Acad. Sci. USA* **2023**, *120*, e2307671120.

Data availability

All data needed to support the conclusions in the paper are presented in the manuscript and the Supplementary Information. Additional data related to this paper may be requested from the corresponding author upon request.

Acknowledgements

M. R M. would like to acknowledge Grantham Centre for Sustainable Futures for providing funding her PhD project, scholarship, and training. The authors also acknowledge Dr. Natalia Sergeeva at University of Leeds, UK, for useful discussions. The authors thank UK HEC Materials Chemistry Consortium which is funded by EPSRC (No. EP/X035859) for computer time on the ARCHER2 UK National Supercomputing Service (http://www.archer2.ac.uk).

Author contributions

M. R. M. – investigation, data curation, formal analysis, project administration, validation, writing – original draft. N. M. – conceptualization, funding acquisition, methodology, investigation, data curation, formal analysis, project administration, supervision, validation, visualisation, writing – original draft, writing – review and editing.

Competing interests

The authors have no competing interests to declare that are relevant to the content of this article.

Use of AI statement

None.

Additional information

Supporting Information The online version contains supplementary material available at https://doi.org/10.26599/CF.2026.9200071.